Materials Research. 2021; 24(6): e20210136
DOI: https://doi.org/10.1590/1980-5373-MR-2021-0136

Effects of Zn Substitution on the Dispersion Spectrum of Permeability and Permittivity of Cu-Mn Ferrites in 1 MHz - 1 GHz Frequency Range

Geraldo T. de Freitas[a*], Rodrigo G. A. de Lima[b], Antonio C. C. Migliano[a,b]

[a]*Instituto Tecnológico de Aeronáutica, 12228-900, São José dos Campos, SP, Brasil.*
[b]*Instituto de Estudos Avançados, 12228-001, São José dos Campos, SP, Brasil.*

Received: March 20, 2021; Revised: September 11, 2021; Accepted: September 19, 2021

This work presents a study of Mn-Zn-Cu triphasic spinel ferrite according to Stoichiometry $Cu_{(0.5-\beta)}$ Zn_{β} $Mn_{0.5}$ Fe_2O_4 with β = 0.10, 0.20, 0.30 and 0.40 . The samples were produced by the conventional ceramic method of sintering, irrigated with partial oxygen pressure, following a determined thermal curve. The morphological, microstructural, dielectric and magnetic properties were characterized by X-ray Diffraction (XRD), Scanning Electron Microscopy (SEM), Energy Dispersive Spectroscopy (EDS) analysis and impedance measurements. The data obtained demonstrated the influence of stoichiometry on the dimensional morphological variation, density, grain size, and electromagnetic behavior in the proposed frequency range. Electromagnetic analysis revealed electrical (ε*) and magnetic (μ*) behaviors very similar to an almost linear decrease of the real and imaginary parts with the increase of frequency, with some oscillations in several parts of the curve, according to the different β. Thus, for the ferrites produced by the conventional ceramic method of powders oxides sintering, irrigated with partial oxygen pressure, within a determined thermal curve, we observed an important relationship between the different triphasic stoichiometric combinations of Mn-Zn-Cu, according to the different β, with their volume, density, grain size, and electromagnetic response in the frequency range from 1.0 MHz to 1GHz.

Keywords: *Ceramics Processing, Electromagnetic Properties, Electronic Materials, Manganese Copper Zinc Ferrites.*

1. Introduction

Cu-Mn ferrites belong to a unique family of ferrites with specific importance due to their high magnetic permeability values and low losses at low frequencies[1]. These features are explored in the development of applications in electronic devices, special cores for transformers, sensors, antennas and miniaturized SMD components, nanotechnologies, and to remove aqueous organics in environmental applications[2-4].

Mn-Cu-Zn ferrite has basically the same electromagnetic properties as Ni-Cu-Zn ferrite. However, the latter is considered more economically interesting because it uses low cost materials and has simpler sintering processes[1,5-7].

Spinel ferrites have been widely used in recent years due to their electromagnetic properties for this form of crystalline structure. This type of ferrite has a general formula AFe_2O_4, where A is bivalent metal ion, e.g., Fe, Mg, Zn, Ni, Mn, Cu, etc. This metal cation A is mounted in the tetrahedral-shaped crystalline structure and with oxygen as a FCC close packaging structure[8,9].

Manganese Ferrite - $MnFe_2O_4$ and mixed ferrites such as $MnFe_2O_4$; $ZnFe_2O_4$; and $CuFe_2O_4$ are recognized as having particular properties of high magnetic permeability (μ*) with high electrical impedance[1,5,10-12]. Considering that these quantities are complex in form: ε* = ε'+ jε'' and μ* = μ' + jμ'', further study is necessary for a perfect understanding of these characteristics. This work proposes to do this, and also it is addressed to the production of a very particular type of Mn ferrite, containing together the elements Cu and Zn. The stoichiometry adopted for Cu-Mn-Zn ferrite was $Cu_{(0.5-\beta)}$ Zn_{β} $Mn_{0.5}$ Fe_2O_4.

From this basic stoichiometry, according to the β, ranging from 0.00 to 0.50, we have six other resulting stoichiometries. In this work the β = 0.00 and 0.50 were disregarded for not having the joint combination of the three elements Cu-Mn-Zn, therefore, outside of the aim of this work. Thus, this work is only directed at β = 0.10; 0.20; 0.30 and 0.40, which are the most relevant stoichiometries for presenting the three-phase combination of the three Cu-Mn-Zn elements.

2. Experimental procedure

Powder metallurgy, commonly referred to as the conventional ceramic oxide powder sintering method, was the method adopted for sample production[13,14]. In this work, we also used, incorporated with this process, the irrigation of partial pressure of oxygen, associated with a specific thermal curve of sintering[15]. The precision of the production method, as well as the care with the values and the control of the variables involved, have a great influence on the quality of the samples produced.

*e-mail: geraldo_tadeu@yahoo.com.br

2.1. Preparation of oxide powders

Two batches of 50 g of sample material were produced. This value was adopted according to the volumetric capacity of the mixing jars in the eccentric metal ball mill. The three-phase Cu-Mn-Zn ferrite powder was synthesized using the conventional solid state reaction of mixed oxide powders from the data shown in Table 1.

The summaries of the stoichiometric calculations used are detailed in Tables 2 and 3.

These oxide powders were mixed with distilled water in an eccentric metal ball mill for 4 hours at a rotation speed of 330 rpm. After grinding, the mixture in suspension was oven dried at 150 °C for 8 h, and the powder was sieved with 115 and 90 μm particle sizes.

The calcination of the oxide mixture was performed at 900 °C for 4 h, with heating and relaxation ramps at a rate of +/- 5 °C min^{-1}, in an environment irrigated with oxygen at 3 liters min^{-1} flow rate at a pressure of 19.61 Pa. This temperature was adopted as an intermediate value of the melting temperatures of the oxides used. Oxygen irrigation was turned on and off at temperatures of 600 °C on the up and down ramps respectively; this value was adopted so that the irrigation with oxygen occurred at the exact moment of the calcination reactions between the oxides. Below this temperature, we are still in the heating process. Therefore, the irrigation with oxygen becomes unnecessary for the reaction. There is an important relationship between oxygen pressure and combustion temperature. Increasing oxygen pressure increases the temperature and consequently the speed of combustion. Thus, there is a lower limit on this pressure to be observed, because the combustion reaction cannot be self-sustaining when the oxygen pressure is below 0.30 MPa[12,16].

2.2. Formation and sintering of samples

In this work, two types of samples were produced, in the forms of toroid and discs, both sintered by the conventional ceramic method of oxide powders sintering, according to:

a) A disk-shaped sample with a diameter of 20 mm and a thickness of 5 mm, — which we call pellets. They were used for microstructure analysis and crystallographic characterization. As shown by Figure 1a.

b) A toroidal sample with 10 mm long, 6.8 mm outside diameter, and 3.1 mm in-side diameter. They were used for electromagnetic characterization. As shown by Figure 1b.

The calcined oxide powders were uniaxially pressed with 40MPa in steel dies for both types of described shapes.

The sintering of both types of samples was performed at 1200 °C for 4h with +/- 5 °C min^{-1} heating and relaxation ramps in a combustion environment irrigated with oxygen at a flow rate of 3 liters min^{-1} at a pressure of 19.61 Pa. This temperature was adopted with a higher value than the melting temperatures of the calcined oxide powders used, in a way to ensure the sintering of the samples. Oxygen irrigation was turned on and off at temperatures of 900 °C on the up and down ramps respectively. This value was adopted so the oxygen irrigation occurred at the exact moment of the sintering reactions between the calcined oxide

Table 1. Summary of oxides used in the production of oxide powders.

Powder oxides	Formula	Manufacturer	Purity	Melting Temperature °C
Iron oxide	Fe2O3	USIMINAS	90%	1566
Zinc oxide	ZnO	VETEC	90%	1975
Copper II oxide	CuO	Labsynth	90%	1201
Manganese oxide	MnO2	VETEC	90%	535

Table 2. Summary of stoichiometric oxide powders calculations for a mass of 50g.

Oxides	β =0.10		β =0.20		β =0.30		β =0.40	
Iron	65.68%	32.84g	65.64%	32.82g	65.58%	32.79g	65.54%	32.77g
Zinc	3.35%	1.675g	6.69%	3.345g	10.04%	5.02g	13.36%	6.68g
Copper II	13.09%	6.545g	9.80%	4.90g	6.53%	3.265g	3.26%	1.63g
Manganese	17.88%	8.94g	17.87%	8.935g	17.85%	8.925g	17.84%	8.92g

Table 3. Summary of the final stoichiometric calculations.

β	Cu	Zn	Mn	Fe	O	Total
0.10	25.418	6.538	27.469	111.690	63.996	235.111 (g/mol)
	10.811	2.780	11.683	47.505	27.219	100 (%)
0.20	19.064	13.076	27.469	111.690	63.996	235.295 (g/mol)
	8.102	5.557	11.674	47.468	27.198	100 (%)
0.30	12.709	19.614	27.469	111.690	63.996	235.478 (g/mol)
	5.397	8.329	11.665	47.431	27.177	100 (%)
0.40	6.355	26.152	27.469	111.690	63.996	235.662 (g/mol)
	2.696	11.098	11.656	47.394	27.156	100 (%)

powders. Below this temperature we are still in the middle of their heating process. Therefore, irrigation with oxygen is unnecessary for the reaction. In studies involving the sintering of Mn-Zn ferrite for use in high frequency power supplies, where core losses are extremely relevant for the optimization of electricity consumption, the doping effect of low partial oxygen pressure was observed during the sintering in the magnetic properties of this type of ferrite. The oxygen used has the function of an FCC packaging structure in the construction of the ferrite spinel structure[15,16]. A low partial oxygen pressure in the sintering atmosphere, along with a temperature curve with the appropriate profile during sintering, decreases the average grain size. This fact reduces the relative eddy current losses due to the higher electrical resistivity of ferrite compared to metals[16].

The surfaces of the sintered pellet samples were prepared by standard metallographic methods. The surfaces of the samples were sanded with sandpaper of the following grades: 240, 320, 600, 800, 1200. They were then polished with diamond pastes of 6 μm, 3 μm, 1 μm and 0.25 μm particle size. The polished samples were thermally attacked at a temperature peak of 1200 °C, with heating and relaxation ramps at a rate of 5 °C min^{-1}. The oxygen irrigation was turned on and off at 900 °C under the same pressure and flow rates conditions already described, in the up and down ramps, for the reasons already mentioned above. The sintered toroidal samples were 10 mm long, with 6.8 mm external diameter, and their internal diameter machined at 3.1 mm.

2.3. Morphological dimensional analysis of pellet samples.

The pellet samples were measured on a DIGIMESS Optical Profile Projector, and their volume was calculated from the collected data[17]. Table 4 presents the results obtained.

The pellet samples were measured and calculated by the Archimedes Method according to the ASTM B962-17 standard[18], using:

$$D_s = \frac{m_{dry}\, d_{water}}{m_{wet} - m_{immersed}} \quad (1)$$

The results are shown in Table 5.

2.4. Analysis by Scanning Electron Microscopy (SEM) and Energy Dispersive Spectroscopy (EDS).

In order to observe the microstructure and chemical composition of the sintered pellet samples, with the surfaces thinned out and thermally attacked, analyses were performed by Scanning Electron Microscopy (SEM), and their chemical composition was mapped by Energy Dispersive Spectroscopy

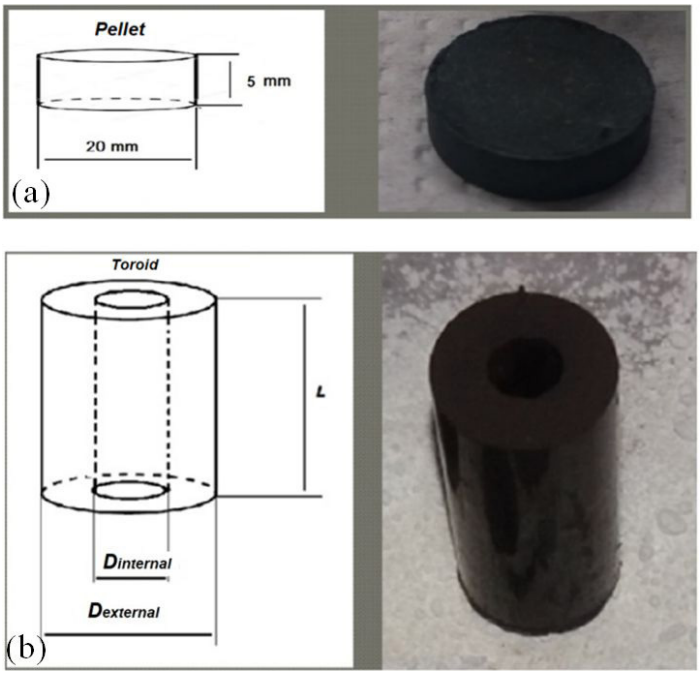

Figure 1. Pellet (a) and Toroid (b) samples.

Table 4. Dimensional measurements of pellet samples.

β	Diameter (mm)	Thickness (mm)	Area (mm2)	Volume (mm3)
0.10	16.12	2.89	204.24	589.83
0.20	16.11	2.90	203.81	590.83
0.30	15.94	2.98	199.60	594.21
0.40	16.61	4.25	216.68	920.89

(EDS), using a TESCAN VEGA3 microscope in the Associated Laboratory of Sensors and Materials (LABAS) of the Brazilian Space Research Institute (INPE).

2.5. X-ray Diffraction Analysis (XRD).

The X-ray Diffractometry (XRD) analysis was performed on sintered pellet samples, with the surfaces thinned out and thermally attacked, using the PANalytical X-ray diffractometer model X'Pert PRO in the Associated Laboratory of Sensors and Materials (LABAS) of the Brazilian Institute for Space Research (INPE). The type of digitization was continuous, the applied current was 40 mA with 45 kV voltage, and a wavelength of $\lambda = 1.54060$ Å (0.15406 nm). The variation of the angle 2θ started at 10.0000 up to the limit of 90.0000. The objective of this analysis was to verify the crystal structure of the samples. The HighScore version 3.05 software was used for phase identification, semiquantitative phase analysis, pattern treatment, and profiling[19].

Lattice Parameters were calculated by Bragg's Law for a cubic system through the following relation:

$$D_{hkl} = \frac{n\lambda}{2Sin(\theta)} \quad (2)$$

And the cubic crystal lattice spacing was calculated according to:

$$a = D_{hkl}\sqrt{h^2 + k^2 + l^2} \quad (3)$$

Considering h, k, and l as the Miller indices of the Bragg's Plan.

2.6. Measurement of electromagnetic properties.

For the measurement of complex magnetic permeability (μ^*) and complex electrical permittivity (ε^*), we used an impedance analyzer model KEYSIGHT E4991B - 1 MHz – 3 GHz, coupled, with coaxial cables, to a magnetic material test fixture (KEYSIGHT 16454A) and a dielectric material test fixture (KEYSIGHT 16453A)[20-22].

All tests were performed at a constant temperature of 20 °C, in the frequency range of 1 MHz – 3 GHz. The pellet samples were used for complex electrical permittivity measurements (ε^*), while the toroid samples were used for complex magnetic permeability measurements (μ^*). For this purpose, the samples were formatted in the dimensions acceptable to the sample holder, as follows: The pellet samples were thinned out to 3.0 mm thickness, while the toroid samples were thinned out to 3.0 mm in length, 6.8 mm external diameter, and their internal diameter machined at 3.1 mm. The arrangement used is shown in Figure 2.

For these complex permeability measurements, the Impedance Method was used[13,23]. The toroid sample impedance was measured from the arrangement shown in Figure 2 using a Magnetic Material Text Fixture KEYSIGHT 164554A, and the results for the complex magnetic permeability (μ^*) were obtained according to:

$$\mu_r^* = \frac{2\pi\left(Z_m^* - Z_{sm}^*\right)}{j\omega\mu_0 h \ln\frac{c}{b}} + 1 \quad (4)$$

Table 5. Results of the mass measurements of the pellet samples in wet, immersed, and dry conditions.

β	Wet mass (g)	Immersed mass (g)	Dry mass (g)	Sintering density (g/ml)
0.10	3.003	2.406	3.003	5.015
0.20	2.838	2.275	2.838	5.022
0.30	5.262	4.218	5.263	5.025
0.40	4.440	3.497	4.362	4.613

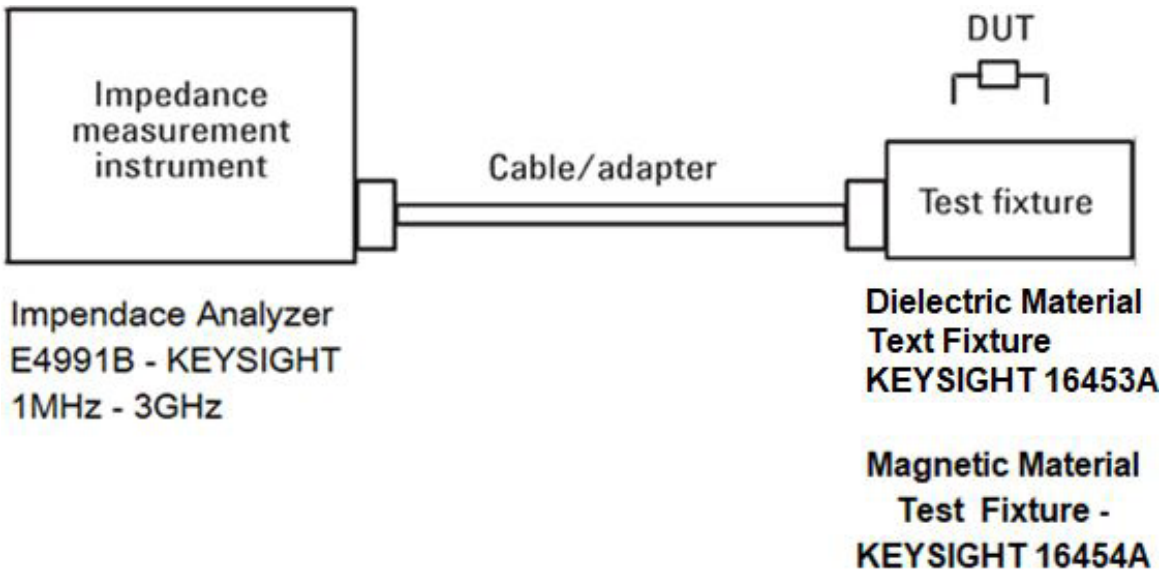

Figure 2. Experimental arrangement for impedance measurements[20-22].

where Z_m^* is the complex impedance measured with the device under test (DUT) mounted on the 16454A fixture test and Z_{sm}^* is the complex impedance measured without the device under test (DUT) mounted on the 16454A fixture test, shorted.

The results for the complex electrical permittivity (ε*) were obtained by the Parallel Plate Method according to:

$$\epsilon_r^* = \frac{4}{\pi}\frac{C_p^* e}{d^2} \quad (5)$$

Where C_p^* is the complex capacitance measured with the device under test (DUT) mounted on the 16453A fixture test, e is the thickness of the pellet sample and d is the diameter of the pellet samples.

3. Results and Discussion

The first results appeared shortly after the samples were sintered. The dimensions and volume of the pellet samples were measured and a lower volumetric decrease was observed in the samples with β = 0.40 ($V_{\beta=0.40}$ = 920.88 mm³), while the others remained practically constant ($V_{average}$ = 591.62 mm³). Figure 3 presents the results obtained.

These dimensional data were later confirmed by the density measurement using the Archimedes Method[18] as shown by Figure 4. We observed that the densities of the samples with β = 0.10; 0.20; and 0.30 remained substantially the same ($D_{average}$ = 5.0205 g/mL). While the sample with β = 0.40 differed from the others, presenting a lower value of 4.6135 g/ml. This is due to lower volumetric decrease that occurred in this sample, and also to a substantially smaller grain size than the other samples. This denotes the influence of the Zn, in greater concentration, in decreasing the grain size of this sample, as shown in Figure 5d and 6d. Also in this sample, Cu was replaced by Zn, because in this stoichiometry the Cu element is in lower concentration than Zn (4.1% and 10.5% respectively)[24]. As indicated by the obtained EDS and XRD results, shown in the Figure 5d and 7d.

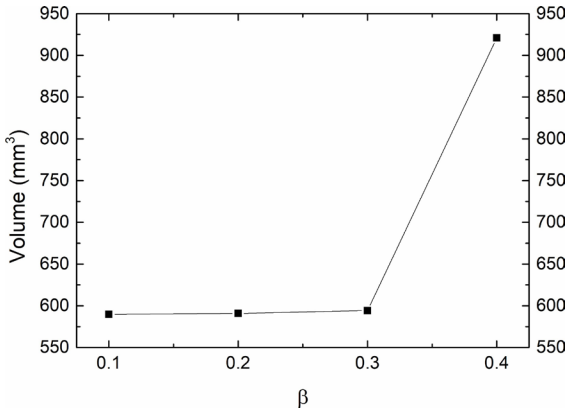

Figure 3. Volume evolution of pellet samples as a function of β.

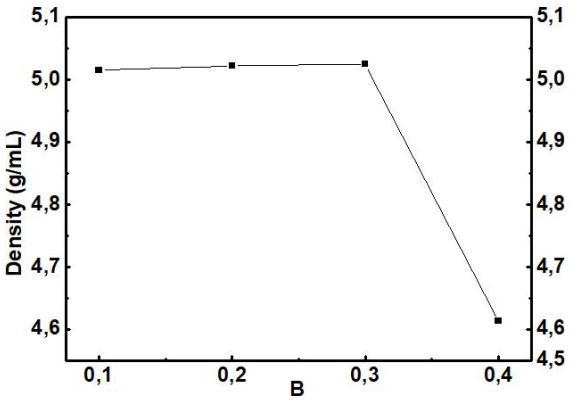

Figure 4. Evolution of the density of pellet samples as a function of β.

The results of the Energy Dispersive Spectroscopy (EDS) analysis confirmed that the stoichiometry was prepared with an error of less than 2.2%. Figure 5 and Table 6 show the results obtained.

The results of the Scanning Electron Microscopy (SEM) analysis demonstrate a uniform crystalline structure with little variation in grain size as a function of the β for the first three samples. A difference appears in the sample with β = 0.40 where the grain size was reduced substantially. The proportion of Mn remained practically constant in all samples; what varied was the proportion of Zn and Cu in each, with the β = 0.40 having less Cu and more Zn. This stoichiometry favored the reduction of grain size, a volume increase of the sintered sample and consequently a lower density in relation to the previous samples. Figure 6 shows the results obtained.

The results of X-ray diffraction (XRD) analysis show one peak near 35° in all samples for the angle 2θ, with reflection indices in the Miller Plane of (311), which characterizes a spinel crystal structure. This is the typical structure of ferrite with Mn[25,26].

Samples with β = 0.20; 0.30 and 0.40 showed a Fe_2O_3 residue that did not react with Cu and Zn. Only the sample with β = 0.10 did not present this residue, which indicates that all Fe_2O_3 iron oxide was absorbed during the sintering process. In samples with β = 0.10 and 0.20, it was observed that Zn was not absorbed due to its low concentration (2% and 6.0% respectively) being replaced by Cu. In samples with β = 0.30 and 0.40 the opposite occurred, i.e., the Cu was replaced by Zn, because in these stoichiometries the Cu element is in lower concentration than Zn (5.4% and 4.1% respectively), as shown in Figure 5.

Table 7 shows the calculated Lattice Parameters results and the cubic crystal grid spacing a.

Based on these calculations and the results of X-ray diffraction (XRD) analysis, we can conclude that the crystal structures of these ferrites are cubic and spinel, as shown in Figure 7.

The results of the electromagnetic properties measurements involving the complex magnetic permeability (μ*) and the complex electrical permittivity (ε*) found several electromagnetic phases in the crystalline molecular microstructure of the samples.

For the sample with β = 0.10 we observed that the complex electrical permittivity (ε*) has its real part (ε') decreasing almost linearly as the frequency increases, and the imaginary part (ε'') follows the same behavior with some oscillation as shown in Figure 8a. The Cole-Cole chart demonstrates

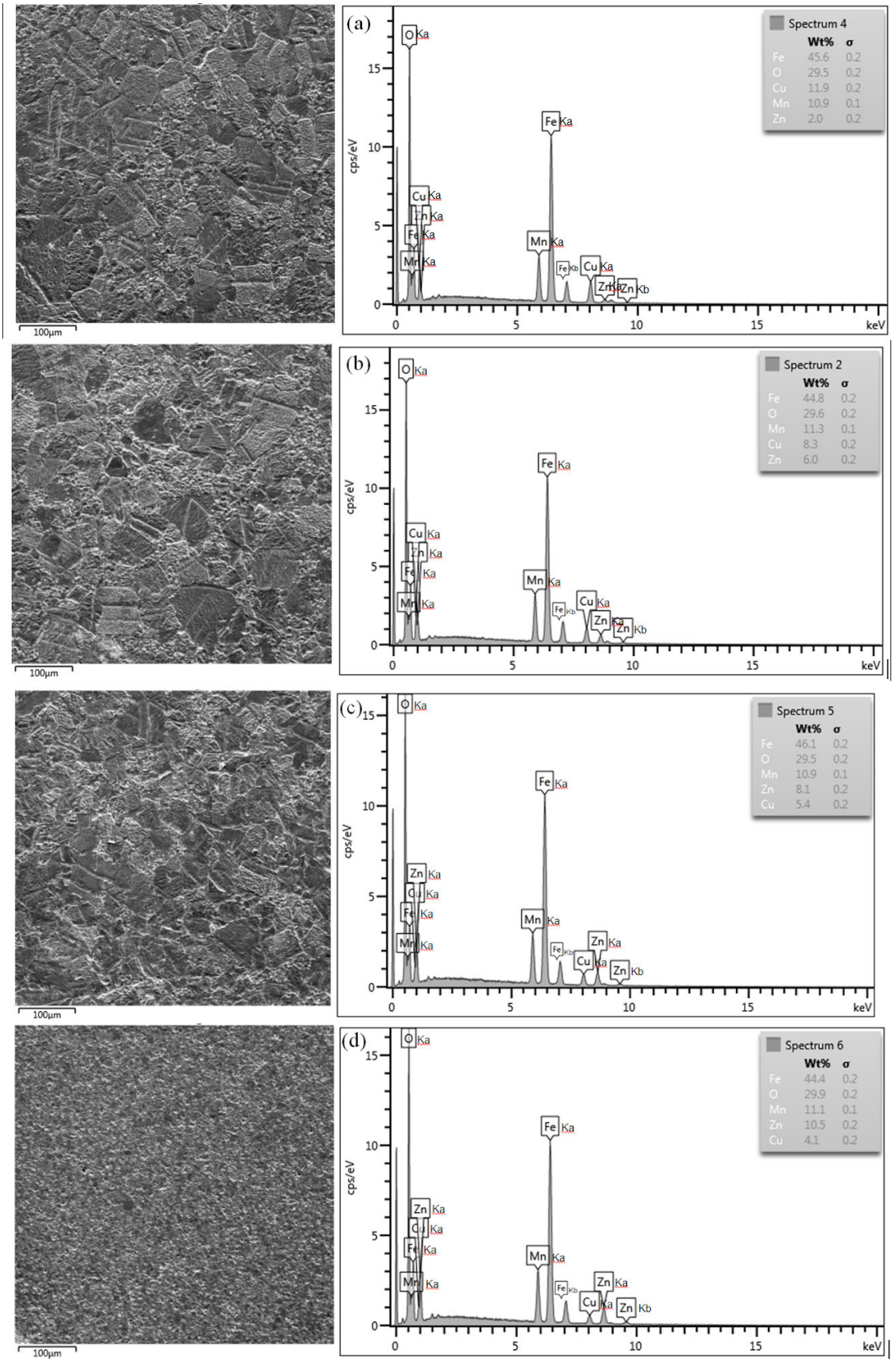

Figure 5. Energy Dispersive Spectroscopy (EDS) analysis for the pellet sample with β = 0.10 (a), 0.20 (b), 0.30 (c) and 0.40 (d).

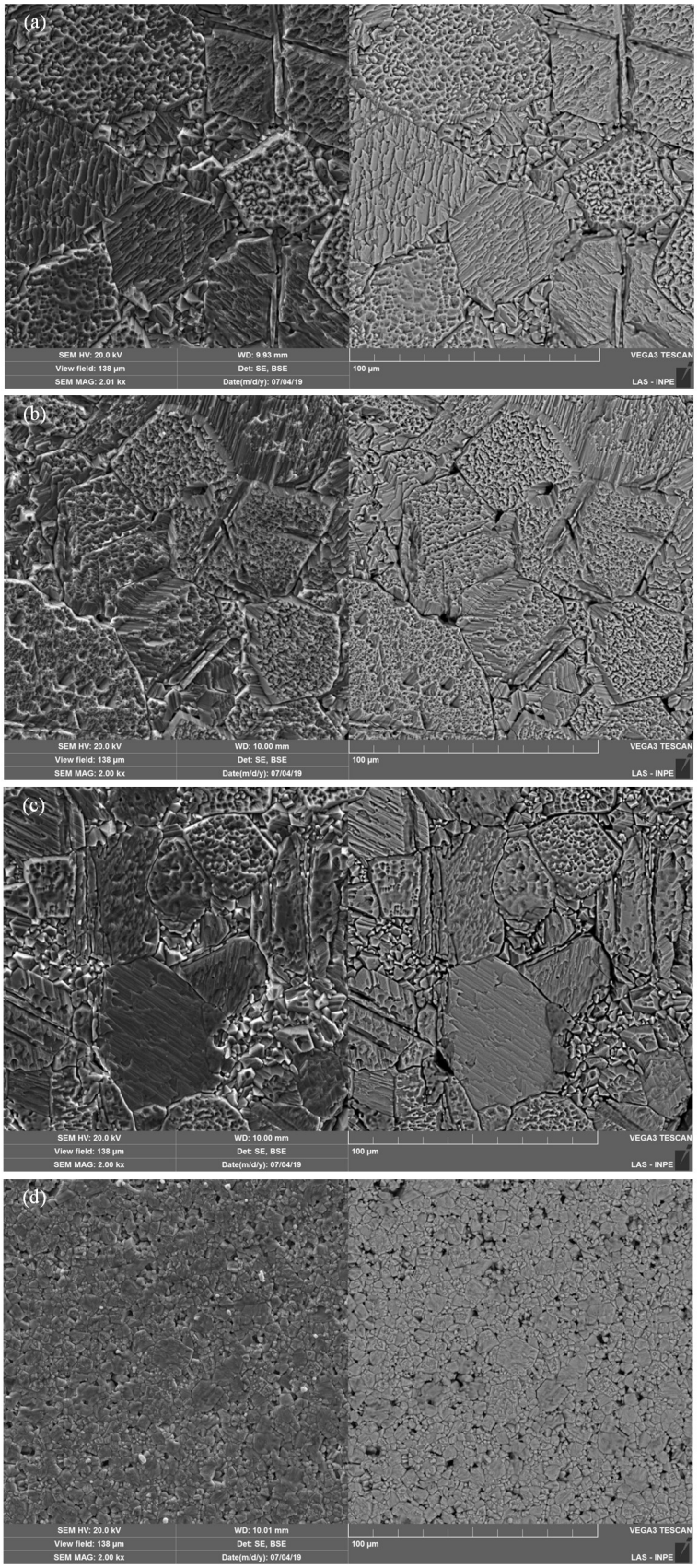

Figure 6. Scanning Electron Microscopy (SEM) analysis for the pellet sample with β = 0.10 (a), 0.20 (b), 0.30 (c) and 0.40 (d).

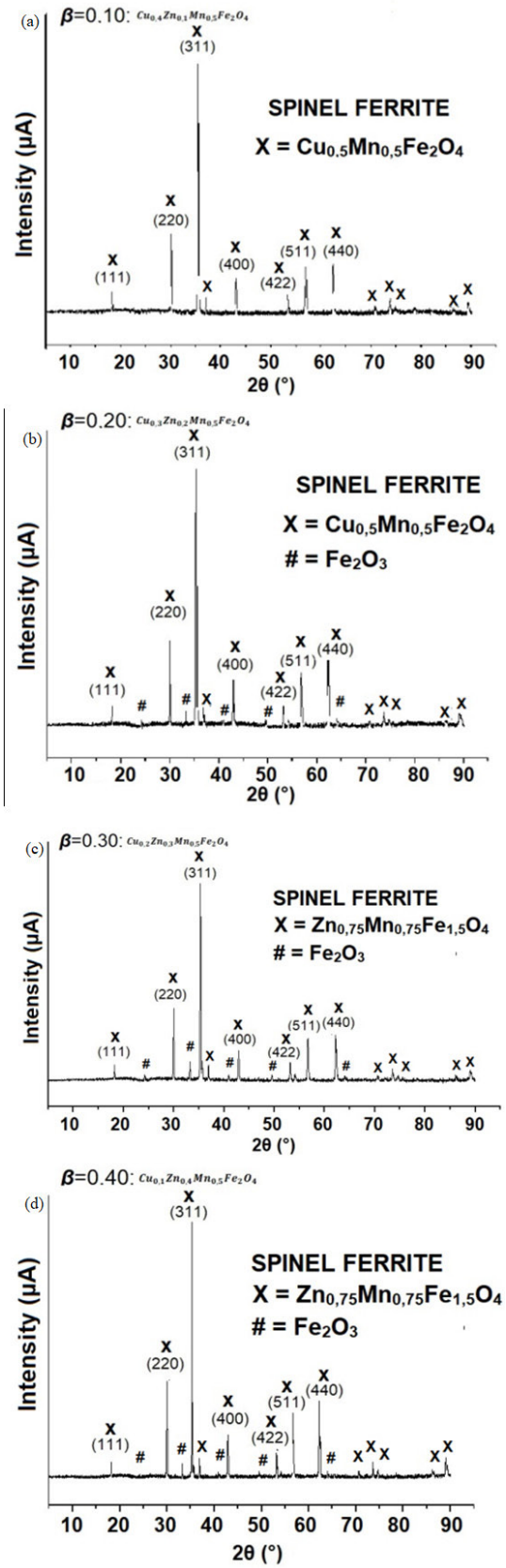

Figure 7. X-ray diffraction (XRD) analysis for the pellet sample with β = 0.10 (a), 0.20 (b), 0.30 (c) and 0.40 (d).

a relaxation frequency (f_R) of 5.1140 MHz[26], as shown in Figure 8b. The magnetic behavior of the sample with β = 0.10 represented by the complex magnetic permeability (μ*) also follows the same decay behavior as the frequency increases. However, it shows larger oscillations in the real part value (μ'), as well as in the imaginary **(μ")**. Figure 8c demonstrates this. These variations, when presented by the Cole-Cole chart, underscore the existence of at least four magnetic phases within the crystalline structure. These phases are determined by the four relaxation frequencies (f_R) of 615.595 MHz, 191.371 MHz, 39.582 MHz and 1.095 MHz as shown in Figure 8d.

For the sample with β = 0.20 we observed that the complex electrical permittivity (ε*) has its real part (ε') decreasing almost linearly as the frequency increases, but around 296.753 MHz there is an inflection point in this trend turning the curve upward with increasing frequency.

The imaginary part (ε") follows an oscillatory behavior, with almost linear intervals, increasing with frequency up to a value close to 10 MHz, then decays with the frequency assuming its minimum value around 296.753 MHz, from which it starts to increase again as frequency increases up to the limit of 1GHz, as shown in Figure 8e. The Cole-Cole graph demonstrates the existence of a relaxation frequency (f_R) at 7.807 MHz where the fall and rise of the real (ε') and imaginary (ε") parts happen synchronously as a function of frequency, as shown in Figure 8f.

Regarding the magnetic behavior, characterized by its magnetic permeability μ*, a sharp oscillatory decay of the real part (μ') with four almost linear intervals was observed. Thus, we have a first, almost linear, descending interval between 1 MHz and 8 MHz, a second interval under the same conditions between 8 MHz and 100 MHz, and a third interval also under the same conditions between 100 MHz and 300 MHz and, finally, a fourth and last interval maintaining the decay of the curve at 300 MHz to 1 GHz.

The imaginary part μ" follows an oscillatory behavior, with five almost linear intervals with the frequency. The first range shows a constant curve between 1 MHz and 4 MHz, the second from 4 MHz to 20 MHz with an upward curve, the third from 20 MHz to 200 MHz with a downward curve, the fourth from 200 MHz to 400 MHz with the same trend and, finally, the fifth from 400 MHz to 1 GHz also maintaining a downward curve, as shown in Figure 8e. The Cole-Cole graph demonstrates the existence of at least three magnetic phases with relaxation frequencies (f_R) of 372.070 MHz, 150.271 MHz, 18.918 MHz as shown in Figure 8f.

For the sample with β = 0.30 we observed that the complex electrical permittivity (ε*) reproduces a behavior similar to the samples with β = 0.20, with very close values, as shown in Figure 8i and 8j. The Cole-Cole graph demonstrates that there is only a single relaxation frequency (f_R) at 5.746 MHz, where the fall and rise of the real (ε') and imaginary (ε") parts happen synchronously as a function of frequency. Similarly the magnetic behavior characterized by its magnetic permeability (μ*) also followed the behavior of samples with β = 0.20, with frequency ranges and the trend of curves very close to this sample, as shown in Figure 8k. The Cole-Cole graph demonstrates the existence of at least three magnetic phases with relaxation frequencies (f_R) of 418.071 MHz

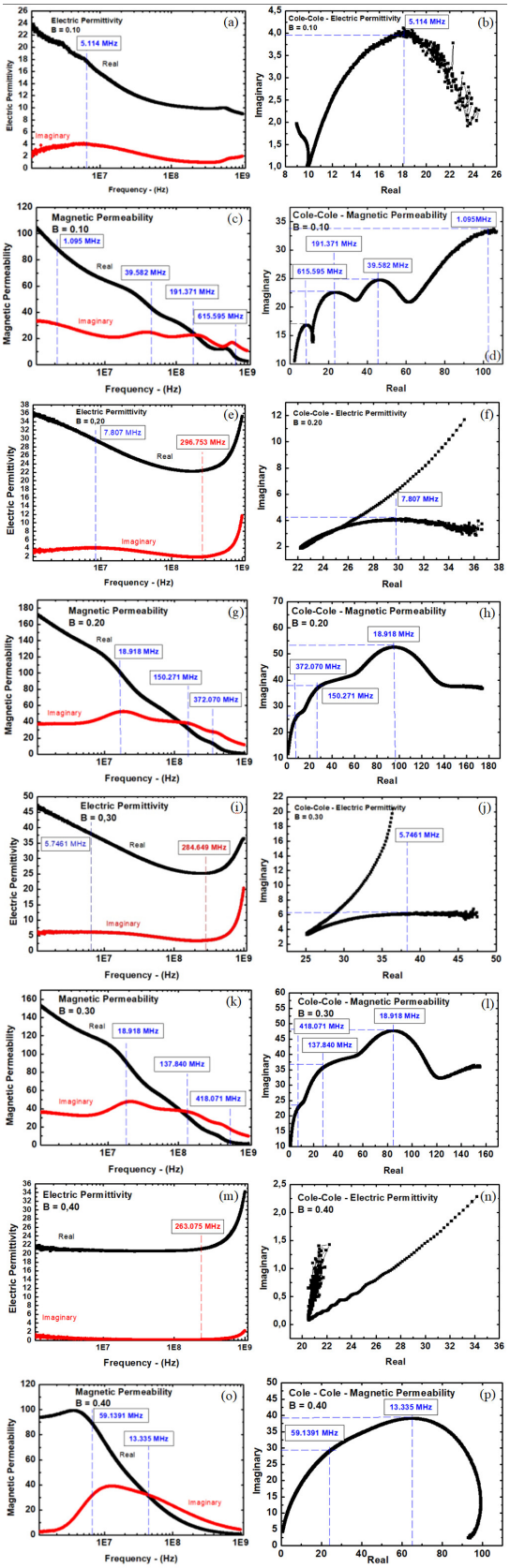

Figure 8. Complex permittivity (ε*) for β = 0.10 (a)(b), 0.20 (e)(f), 0.30 (i)(j) and 0.40 (m)(n) and complex permeability for β = 0.10 (c) (d), 0.20 (g)(h), 0.30 (k)(l) and 0.40 (o)(p).

Table 6. Comparison between the theoretical stoichiometric calculations and the experimental results obtained by the EDS analysis.

β	Method	Cu (%)	Zn (%)	Mn (%)	Fe (%)	O (%)	Total (%)
0.10	Calculated	10.811	2.781	11.683	47.505	27.219	100.000
	EDS	11.900	2.000	10.900	45.600	29.500	99.900
	Error	10.072	-20.887	-1.570	-1.485	-6.317	-2.099
0.20	Calculated	8.102	5.558	11.674	47.468	27.198	100.000
	EDS	8.300	6.000	11.300	44.800	29.600	98.500
	Error	4.913	2.568	9.642	-2.461	-7.347	-1.500
0.30	Calculated	5.397	8.329	11.665	47.431	27.177	100.000
	EDS	5.400	8.100	10.900	46.100	29.500	98.000
	Error	-1.1799	-3.955	1.155	-0.487	-5.435	-1.999
0.40	Calculated	2.695	11.098	11.656	47.394	27.156	100.000
	EDS	4.100	10.500	11.100	44.400	29.900	97.800
	Error	33.509	-9.888	8.098	-1.676	-7.939	-2.200

Table 7. Lattice Parameters Calculation and Cubic Crystal Grid Spacing a. Considering n = 1 and λ = 1.54060 Å.

h	k	l	2θ (°)	Dhkl (nm)	ahkl (nm)
1	1	1	18	0.1869	0.3237
2	2	0	30	0.1185	0.3350
3	1	1	35	0.0790	0.2619
4	0	0	44	8.7027	34.8107
4	2	2	54	0.0810	0.3946
5	1	1	56	0.2843	1.4775
4	4	0	62	0.1907	1.0785

Table 8. Summary of samples characteristics.

β	Stoichiometry	Volume (mm3)	Density (g/ml)	Dielectric relaxation frequency (MHz)	Magnetic relaxation frequency (MHz)
0.10	Cu0.4Zn0.1Mn0.5Fe2O4	589.831	5.0149	5.114	1.095
					39.582
					191.371
					617.595
0.20	Cu0.3Zn0.2Mn0.5Fe2O4	590.829	5.0221	7.807	18.918
					150.271
0.30	Cu0.2Zn0.3Mn0.5Fe2O4	594.212	5.0245	5.748	18.918
					418.071
					137.840
0.40	Cu0.1Zn0.4Mn0.5Fe2O4	920.884	4.6135	None	13.335
					59.139

137.840 MHz and 18.918 MHz. There may be a fourth phase below this frequency, but for now we cannot confirm it with our experiments, as shown in Figure 8l. Samples with β = 0.20 and 0.30 are equivalent in their electromagnetic behavior in pragmatic terms.

Finally, the sample with β = 0.40 presents a completely different electromagnetic behavior than the other samples. Thus, we observed that the complex electrical permittivity (ε*) has its real (ε') and imaginary (ε'') parts practically constant with increasing frequency up to approximately 263.075MHz**.** This value for both curves has an upward inflection, with the real part (ε ') being more pronounced graphically, but the imaginary part (ε'') also follows the same values observed, as shown in Figure 8m. The Cole-Cole graph demonstrates this linearity between the real (ε') and imaginary (ε'') parts, as shown in Figure 8n. The magnetic behavior, characterized by its magnetic permeability (μ*), is formed by almost linear intervals of ascending and descending curves. The variation of the real part (μ') as a function of frequency occurs in at least three almost linear intervals. The first interval between 1 MHz and 3 MHz has an upward variation with the frequency. The second range between 3 MHz and 100 MHz has a sharp downward variation with the frequency, and the third and last range between 3 MHz and 1 GHz also has a milder downward curve. Similarly, the variation of the imaginary part (μ'') with frequency presents at least four almost linear ranges of variation. The first interval from about 1 MHz to about 1.5 MHz has a slightly upward curve. The second between 1.5 MHz and 10 MHz has a steeper upward curve, the third between 10 MHz and 50 MHz has a downward curve, and the fourth and last between 50 MHz and 1 GHz also has a downward curve, as shown in Figure 8o. These variations when presented by the Cole-Cole chart demonstrate the assertive existence of at least two magnetic phases within the crystalline structure, with relaxation frequencies (f_R) of 13.335 MHz and 59.1391 MHz. The EDS and XRD results demonstrate that Zn substantially replaced Cu in the ferrite crystal structure of this sample[27]. And this produced a differentiated electromagnetic behavior compared to other samples with different stoichiometry[28,29]. As shown in Figure 8p.

Table 8 summarizes the main characteristics identified in the samples according to β.

4. Conclusion

In this work, Mn-Cu-Zn ferrites, with different stoichiometries, were produced using conventional ceramic method.

The dimensional morphological and density measurements of the samples showed that ferrites with β = 0.10, 0.20 and 0.30 had similar values for volume and density ($V_{average}$ = 591.6243 mm^3 and $D_{average}$ = 5.0205 g/ml). However, the sample with β = 0.40 presented a higher volume and, consequently, lower density ($V_{\beta 0.40}$ = 920,8847 mm^3 and $D_{\beta 0.40}$ = 4.6135 g/ml).

EDS and XRD analysis showed that in samples with β = 0.30 and 0.40, Cu was replaced by Zn, as shown by the lower concentration of Cu compared to Zn. In the samples with β = 0.10 and 0.20 the opposite behavior occurred, Zn has lower concentration than Cu.

The images of the molecular microstructure of the samples revealed by Scanning Electron Microscopy (SEM) analysis showed a nearly equal grain size for samples with β = 0.10, 0.20 and 0.30. However, the sample with β = 0.40 has a substantially smaller grain size than the other samples, denoting the influence of the Zn in decrease of the grain size of this sample.

X-ray diffraction (XRD) analysis also showed the existence of Fe_2O_3 residue in samples with β = 0.20, 0.30 and 0.40. Only the sample with β = 0.10 had all the iron oxide absorbed. This may be resolved by an increase in the value of the calcination temperature used.

Samples with β = 0.10, 0.20 and 0.30 showed similar magnetic behavior, with an almost linear decrease of the real part of permittivity with frequency. The imaginary part also follows the same behavior, but with some differences according to the β. The Cole-Cole curves of all these samples demonstrate several magnetic phases characterized by various relaxation frequencies. While in the sample β = 0.40, the magnetic behavior of its real and imaginary parts rises at the beginning and then decreases almost linearly with increasing frequency. The Cole-Cole curve presented two determined relaxation frequencies (f_R), denoting two magnetic phases within the crystal structure.

The electrical behavior of these samples also followed the same similarity. All of them had an almost linear decrease of their real part of permissivity with increasing frequency to the curve's inflection point at the end of the frequency range. Only the sample with β = 0.10, which is the only one with no Fe_2O_3 residues, did not show this inflection in its curve, maintaining its decreasing inclination in the studied frequency range. Only the sample with β = 0.40 presents a different electric behavior.

5. Acknowledgments

The authors acknowledge the support received from the following professionals and institutions: Dra. Miriam Kasumi Hwang Yassuda, Dr. Franscisco Eduardo de Carvalho and Dra. Mayara dos Santos Amarante, from Institute for Advanced Studies - IEAV, Brazil, for the affection, attention and precious information for the execution of this work. And also to Dr. João Paulo Barros Machado of the Associated Laboratory of Sensors and Materials (LABAS) of the Brazilian Institute for Space Research (INPE).

6. References

1. Ramay SM, Rafique HM, Aslam S, Siddiqi SA, Atiq S, Saleem M, et al. Structural, morphological, and magnetic characterization of sol-gel synthesized MnCuZn ferrites. IEEE Trans Magn. 2014;50(8):1-4.
2. Xian G, Kong S, Li Q, Zhang G, Zhou N, Du H, et al. Synthesis of spinel ferrite MFe2O4 (M = Co, Cu, Mn, and Zn) for persulfate activation to remove aqueous organics: effects of m-site metal and synthetic method. Front Chem. 2020;177:8.
3. Thakur P, Chahar D, Taneja S, Bhalla N, Thakur A. A review on MnZn ferrites: synthesis, characterization and applications. Ceram Int. 2020;46(10):15740-63.
4. Saha P, Debnath T, Das S, Chatterjee S, Sutradhar S. β-Phase improved Mn-Zn-Cu-ferrite-PVDF nanocomposite film: a metamaterial for enhanced microwave absorption. Mater Sci Eng B. 2019;245:17-29. http://dx.doi.org/10.1016/j.mseb.2019.05.006.
5. Lucas A, Lebourgeois R, Mazaleyrat F, Laboure E. Temperature dependence of core loss in cobalt substituted Ni-Zn-Cu ferrite. J Magn Magn Mater. 2011;323(6):735-9. http://dx.doi.org/10.1016/j.jmmm.2010.10.037.
6. Sharma A, Harmanpreet H. Influence of different substitution metal ion on magnetic properties of Mn-Zn ferrite. Mater Today Proc. 2020;37:3058-60.
7. Alam F, Rahman ML, Das BC. Effect of Cu2+ on structural, elastic and magnetic properties of nanostructured Mn-Zn ferrite prepared by a sol-gel auto-combustion method. Physica B. 2020;594:412329.
8. Oliveira VD, Rubinger RM, Silva MR, Oliveira AF, Rodrigues G, Ribeiro VAS. Magnetic and electrical properties of $Mn_xCu_{(1-x)}Fe_2O_4$ ferrite. Mater Res. 2016;19(4):786-90.
9. Narang SB, Pubby K. Nickel spinel ferrites: a review. J Magn Magn Mater. 2021;519:167163.
10. Mohanty D, Mallick P, Biswal SK, Behera B, Mohapatra RK, Behera A, et al. Investigation of structural, dielectric and electrical properties of ZnFe2O4 composite. Mater Today Proc. 2020;33:4971-5.
11. Shetty K, Renuka L, Nagaswarupa HP, Nagabhushana H, Anantharaju KS, Rangappa D, et al. A comparative study on CuFe2O4, ZnFe2O4 and NiFe2O4: morphology, impedance and photocatalytic studies. Mater Today Proc. 2017;4:11806-15.
12. Jabbar R, Sabeeh SH, Hameed AM. Structural, dielectric and magnetic properties of Mn+2 doped cobalt ferrite nanoparticles. J Magn Magn Mater. 2020;494:165726. http://dx.doi.org/10.1016/j.jmmm.2019.165726.
13. Amarante MS, Silva Júnior EO, de Lima RGA, Lente MH, Machado JPB, Migliano ACC, et al. Sintering behavior and electromagnetic properties of a Ni–Co ferrite/NiO biphasic ceramic. Mater Res Express. 2019;6(7):076110.
14. Zheng Y, Jia L, Xu F, Wang G, Shi X, Zhang H. Microstructures and magnetic properties of low temparature sintering NiCuZn ferrite ceramics for microwave applications. Ceram Int. 2019;45(17):22163-8.
15. Znidarsic A, Drofenik M. Influence of oxygen partial pressure during sintering on the power loss of MnZn ferrites. IEEE Trans Magn. 1996;32(3):1941-5. http://dx.doi.org/10.1109/20.492890.
16. Goldman A. Modem ferrite technology. New York: Van Nostrand; 2010.
17. DIGIMESS Precision Instruments Ltda. Profile projector manual 400.400. São Paulo; 2018.
18. American Society for Testing and Materials – ASTM. ASTM B962-17: standard test methods for density of compacted or sintered Powder Metallurgy (PM), products using archimedes' principle. West Conshohocken: ASTM; 2019.
19. PANalytical. HIGHSCORE - X-ray-diffraction-software, version 3.05. Almelo, Netherlands: PANalytical B.V.; 2012.
20. Agilent Technologies. Impedance measurement handbook. USA: Agilent Technologies, Inc.; 2009.

21. Keysight Technologies. Keysight 16453A: dieletric material test fixture: operation and service manual. Hyogo: Keysight Technologies; 2017.
22. Keysight Technologies. Keysight 16454A: magnetic material test fixture operation and service manual. Hyogo: Keysight Technologies; 2017.
23. Lima RGA, Brito VLO, Lemos LV, Migliano ACC. Temperature sensibility of complex permittivity in Ni–Zn ferrite at different temperatures in the 700 MHz–1 GHz range. IEEE Trans Magn. 2018;54(2):1-5.
24. Islam RA, Priya S. Progress in dual (piezoelectric-magnetostrictive) phase magnetoelectric sintered composites. multiferroic magnetoeletric composites and their applications. Adv Condens Matter Phys. 2012;2012:320612.
25. Stergiou C. Magnetic, dielectric and microwave absorption properties of rare earth doped Ni–Co and Ni–Co–Zn spinel ferrites. J Magn Magn Mater. 2017;426:629-35.
26. Callister WD, Rethwisch DG. Materials science and engineering: an introduction. 9th ed. New York: Wiley; 2014.
27. Hassadee A, Jutarosaga T, Onreabroy W. Effect of zinc substitution on structural and magnetic properties of cobalt ferrite. Procedia Eng. 2012;32:597-602.
28. Radoń A, Hawełek Ł, Łukowiec D, Kubacki J, Włodarczyk P. Dielectric and electromagnetic interference shielding properties of high entropy Zn,Fe,Ni,Mg,Cd) Fe2O4 ferrite. Sci Rep. 2019;9(1):20078.
29. Bahadur S, Hossain MA, Sikder SS, Akhter MS. Structural, magnetic and transport properties of Fe-deficient of Ni-Cu-Zn ferrites. Int J Eng Inf Syst. 2017;1:11-27.